Minimalist Design for Solar Energy Conversion: Revamping the π-Grid of an Organic Framework into Open-Shell Superabsorbers

Zhiqing Lin, Yuan-Hui Zhong, Leheng Zhong, Xinhe Ye, Lai-Hon Chung,* Xuanhe Hu, Zhengtao Xu,* Lin Yu, and Jun He*

ACCESS | 📊 Metrics & More | 📖 Article Recommendations | ⓈⒾ Supporting Information

ABSTRACT: We apply a versatile reaction to a versatile solid: the former involves the electron-deficient alkene tetracyanoethylene (TCNE) as the guest reactant; the latter consists of stacked 2D honeycomb covalent networks based on the electron-rich β-ketoenamine hinges that also activate the conjugated, connecting alkyne units. The TCNE/alkyne reaction is a [2 + 2] cyclo-addition−retroelectrocyclization (*CA-RE*) that forms strong push−pull units directly into the backbone of the framework—*i.e.*, using only the minimalist "bare-bones" scaffold, without the need for additional side groups of alkynes or other functions. The ability of the stacked alkyne units (*i.e.*, as part of the honeycomb mass) to undergo such extensive rearrangement highlights the structural flexibility of these covalent organic framework (COF) hosts. The

COF solids remain porous, crystalline, and air-/water-stable after the *CA-RE* modification, while the resulting push−pull units feature distinct open-shell/free-radical character, are strongly light-absorbing, and shift the absorption ends from 590 nm to around 1900 nm (band gaps from 2.17−2.23 to 0.87−0.95 eV), so as to better capture sunlight (especially the infrared region which takes up 52% of the solar energy). As a result, the modified COF materials achieve the highest photothermal conversion performances, holding promise in thermoelectric power generation and solar steam generation (*e.g.*, with solar-vapor conversion efficiencies >96%).

KEYWORDS: *covalent organic framework, post-synthetic modification, photothermal conversion, solar thermoelectric generation*
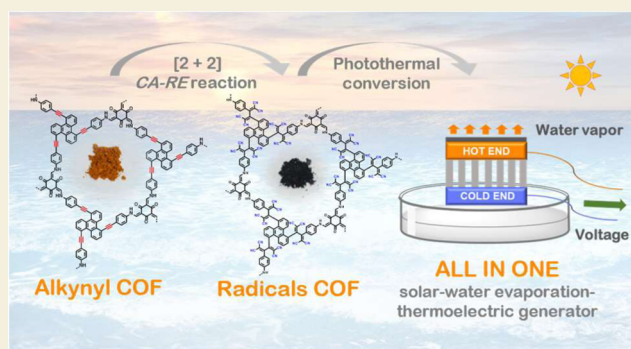
INTRODUCTION

Post-synthetic modification (PSM) represents a major thrust in the study of porous solids of covalent and coordination frameworks (aka COFs and MOFs).[1−6] Therein, the organic linker units allow the open channels to be conveniently varied in size and function. Often, functional side arms are attached to the backbone of the linker molecule, so as to be reacted—in the assembled framework—with incoming guest reagents. A cross-linking reagent, for example, can covalently bridge the individual linkers and serves to convert a coordination framework into a stronger and more stable covalent grid.[7−13] With select side arms and guests, one can even build conjugated bridges (*e.g.*, alkene, oligothiophene, and metal-thiolate)[14−19] to boost the electronic interaction across the organic linker molecules, achieving better conductive and catalytic properties.

Besides the side arms, the backbone of the organic linker molecule can also undergo a structural rearrangement in the solid-state framework,[20−24] with the addition of Br₂ onto the alkyne or alkene units of the backbone being well studied.[25−31] However, transformation of the backbone is generally more difficult because the backbone atoms are more constricted by the rigid framework and therefore less prone to rearranging

their atomic positions (this differs from the side arm, which, dangling off the scaffold, is more free to move around). An illustrative (and somewhat related) case is the topochemical polymerization of diacetylenes in close-packed crystals, which entails close alignment of the reacting units in the solid state.[32−40] In an open framework, the backbone atoms are more accessible than in the close-packed topochemical systems, but still some coordinated motion of the atoms throughout the extended framework is required for the transformation to proceed. So, PSM studies normally target the freer side groups instead. But framework dynamics and flexibility are not to be underestimated, and the above-mentioned Br₂ additions already suggest the great potential of the backbone to react and reshape. Moreover, changes on the linker backbone (especially its π-system) often directly and more deeply impact the solid-state properties. So, it is perhaps

time to shift some attention back to the backbone and exploit its reactivity for functionalization; for example, even in the studied case of the backbone alkyne unit, it is of fundamental interest to simply ask how far one can go beyond the simple bromination.

Presented here is a dramatic revamping of the backbone alkyne units of an ordered covalent organic framework system. Compared with Br_2 addition, the guest reactant here is bulkier, and the reaction is more elaborate, i.e., the electrophilic tetracyanoethylene (TCNE) reacts with the electron-rich alkyne units of the backbone, proceeding in the $[2 + 2]$ cycloaddition–retroelectrocyclization (CA-RE) mechanism[41,42] (Scheme 1) and establishing strongly light-absorbing

Scheme 1. $[2 + 2]$ CA-RE Reaction between the Alkyne and TCNE
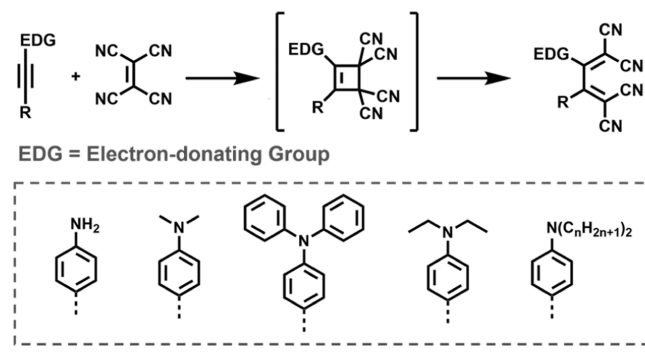
push–pull functions to boost the photothermal conversion performances of the framework solids. These deep linker transformations unveil a surprising degree of flexibility of the organic frameworks to reshape and reform. They point to broad applicability. For example, the host net is efficiently constructed from modular aldehyde and amine building blocks (to form the imine/β-ketoenamine hinges), whose metric and functional diversity[43–47] is highlighted by the gigantic pore sizes of the COF reported recently by Feng et al.[48] on this class of COF materials. The CA-RE reaction[41,42,49–55] is also versatile for the PSM, as various electron-deficient alkene reactants (i.e., besides TCNE) can be tested on the amine-activated backbone alkynes, and the resulting push–pull groups can also undergo further transformations[56–67] to broaden the functional scope.

RESULTS AND DISCUSSION

Synthesis and Characterization of COF–Ss

The synthesis of the framework COF–S1 was recently reported, while COF–S2 is new. The amines (S1 and S2) and the aldehyde (1,3,5-triformylphloroglucinol: Tp) as building blocks feature the tritopic shape to generate the honeycomb net. To promote the crystallinity of the COF products (i.e., COF–S1 and COF–S2; see Figure 1), the monotopic aniline was added as a modulator (see the Supporting Information for detailed synthetic procedures). Compared with the benzenoid core of S1, the triphenylene core of S2 offers a larger, fused-ring π-system for tuning the electronic properties. The three hydroxyl (−OH) groups on the Tp molecule are strongly electron-donating, and they can enhance the electron density of the alkyne units of the COF grid (e.g., by tautomerizing to the β-ketoenamine form, Schemes S5 and S6) and promote the CA-RE reaction with

the electrophilic TCNE guests. In general, amino-activated alkyne functions were found to most effectively undergo the CA-RE reaction—often in a quantitative, "click-like" fashion. As an illustrative model reaction, molecule S1 can react with TCNE even at room temperature to form the expected CA-RE product S1-T (Scheme S3).

Powder X-ray diffraction (PXRD) patterns demonstrate high crystallinity of the COF–S1 (Figure 2a) and COF–S2 solids (Figure 2b). Reasonable R_{WP} and R_p values based on Pawley refinement reveal both COF solids to be of 2D hexagonal sheets in the AA stacking mode (COF–S1: $a = 23.18$ Å and $c = 3.52$ Å and COF–S2: $a = 23.19$ Å and $c = 3.50$ Å, with c corresponding to the interlayer spacing, Figures S15 and S17). The Brunauer–Emmett–Teller (BET) surface areas of COF–S1 and COF–S2 based on N_2 sorption isotherms (Figure 2c) measured at 77 K were found to be 1061 and 630 m^2 g^{-1}, respectively, with pore sizes of around 1.786 and 1.725 nm (Figures S16 and S18), respectively. Importantly, C=O stretching, C=C stretching, and C−N vibrational bands at 1618, 1568, and 1289 cm^{-1} observed in the Fourier-transform infrared (FT-IR) spectrum of COF–S2 (Figure S19) support the formation of the β-ketoenamine links from enol–keto tautomerization. Also, the C≡C stretching at 2181 cm^{-1} indicates that the alkynyl groups are preserved in the COF product. The β-ketoenamine linkage of COF–S2 was also probed by solid-state ^{13}C NMR spectroscopy (139.0, 98.8, and 176.1 ppm for the enamine carbon =C−N, α-enamine carbon C=C, and keto carbon C=O, respectively) and X-ray photoelectron spectroscopy (XPS) (C−N, 400 eV in N 1s spectra) (Figures S20 and S27), as is previously verified for COF–S1.[68]

Synthesis and Characterization of COF–Ss-T

Based on a reported method,[24] the solids of COF–S1 and COF–S2 were reacted with TCNE vapor at 140 °C under vacuum, along with the TCNE reactant replenished twice to ensure complete conversion of the alkyne groups in the COF solids (Figure 1c and Scheme S7). The orange COF–S1 and orange-red COF–S2 powders both became black (Figure S31) after the TCNE treatment. Scanning electron microscopic (SEM) images show that the COF–S1 and COF–S2 particles retain their morphologies throughout the CA-RE reaction (Figure S32). While both COF–S1 and COF–S2 feature weak C≡C stretching at 2200 and 2181 cm^{-1} in the FT-IR spectra, respectively, the TCNE-treated solids of COF–S1-T and COF–S2-T feature prominent peaks of C≡N stretching at 2211 and 2208 cm^{-1} instead, respectively, indicating the reaction of the alkyne functions with the TCNE guests (Figure 2e). Most notably, the solid-state ^{13}C NMR C≡C peaks, while exhibited by COF–S1 and COF–S2 (81 and 84 ppm, respectively), become absent in the spectra of COF–S1-T and COF–S2-T (Figure 2f), indicating the complete reaction of the alkyne groups by the TCNE guests; COF–S1-T and COF–S2-T also feature new peaks (90 and 94 ppm, respectively) consistent with the nitrile groups. The C≡N presence was further confirmed by XPS N 1s spectra (binding energies of 399.7 and 399.5 eV for COF–S1-T and COF–S2-T, respectively), with peak areas greater than those of C−N bonds (Figures S24 and S28). Moreover, the elemental analysis results agree with calculated results (Tables S1 and S2).

After the TCNE treatment, PXRD patterns reveal increased intensity of the (110) peak (at 7.70°) relative to the (100) peak (at 4.40°) for the resulting solids of COF–S1-T ($a = b =$
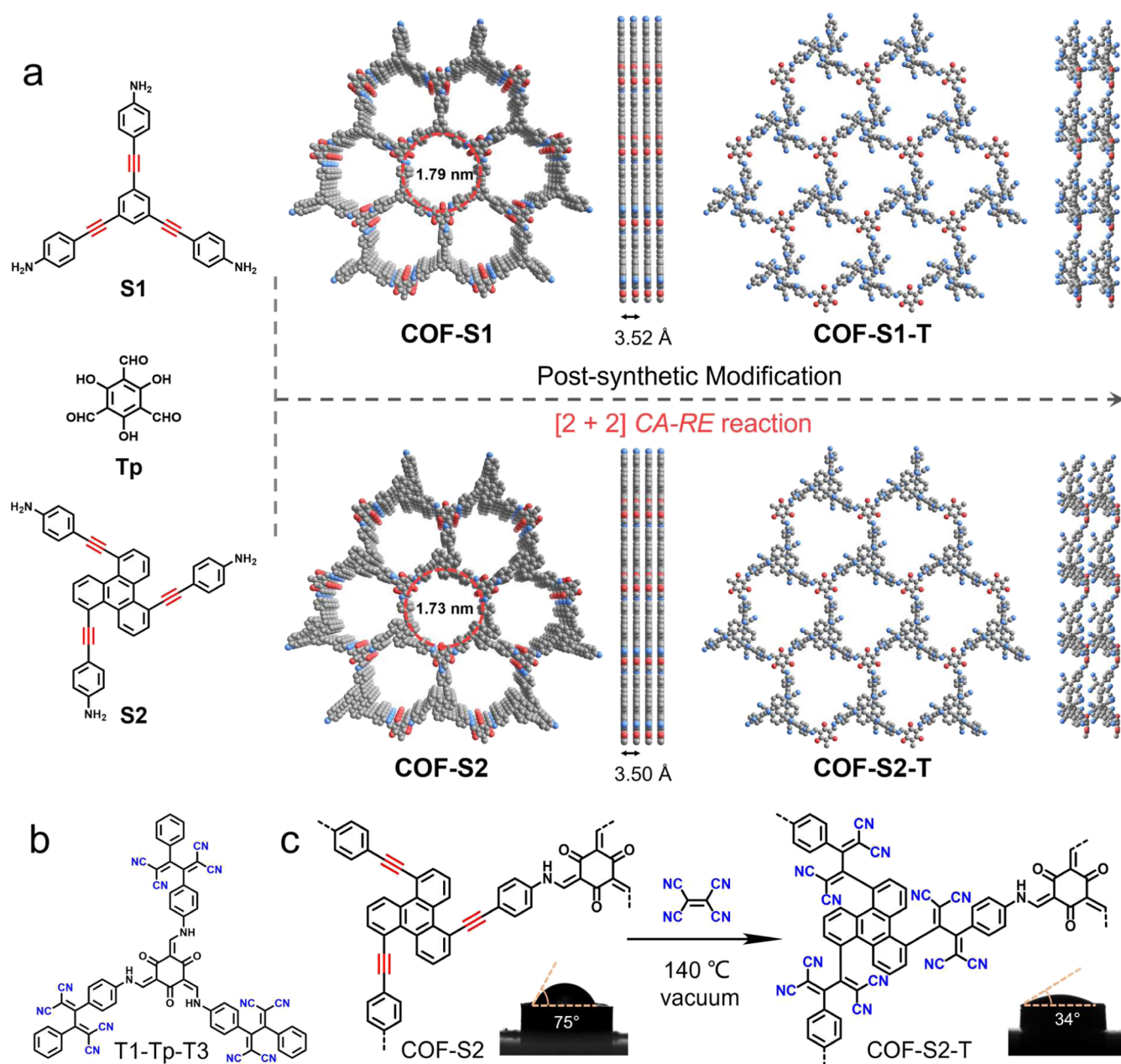
Figure 1. (a) Molecular building blocks and the structural models for COF−S1 and COF−S2 solids and the models for their TCNE-modified derivatives COF−S1-T and COF−S2-T. (b) Model compound T1−Tp−T3. (c) Schematics of reacting TCNE with COF−S2 to form COF−S2-T (with the TCBD function), with two insets showing the water contact angles of COF−S2 and COF−S2-T.

22.11 Å and c = 7.04 Å) and COF−S2-T (a = b = 22.90 Å and c = 8.45 Å, Figures 2d and S29). Both COF−S1-T and COF−S2-T adopt the AA stacking mode on the basis that their precursors (COF−S1 and COF−S2) adopt the same stacking mode, yet with longer interlayer distances in both COF−S1-T and COF−S2-T. To further verify the structural models of TCNE-treated COF−S1 and COF−S2, the Pawley refinements in the AA stacking mode against the experimental PXRD patterns give satisfactory agreement factors (for COF−S1-T: R_{WP} = 3.04% and R_p = 2.3%; for COF−S2-T: R_{WP} = 2.3% and R_p = 1.7%), further indicating the correctness of the AA stacking structural models. In general, crystallinity decreases from COF−Ss to COF−Ss-T (i.e., reflected by weakening and broadening of the PXRD signal, Figure 2a,b,d) because the incorporation of sterically bulky tetracyanobuta-

diene (TCBD) moieties promotes partial amorphization of the frameworks. For COF−S1-T, the (100) peak remains stronger than the (110) peak, but for COF−S2-T, the increase is greater, with (110) now stronger than (100). Such intensity changes suggest that COF−S2-T with the windmill-like triphenylene core crowds more against the neighboring groups, making for less flat shapes and looser stacks when compared with COF−S1-T.[69,70] Generally, a weaker (100) peak relative to (110) indicates more blocking of the hexagonal channels and diminished porosity, which is consistent with the smaller surface area of COF−S2-T relative to COF−S1-T, namely, CO_2 sorption isotherms collected at 273 K indicated BET surface areas of COF−S1-T and COF−S2-T to be 102.80 and 55.53 m^2 g^{-1}, respectively (Figure S36). Incidentally, N_2 uptakes at 77 K for both COF−S1-T and COF−S2-T are
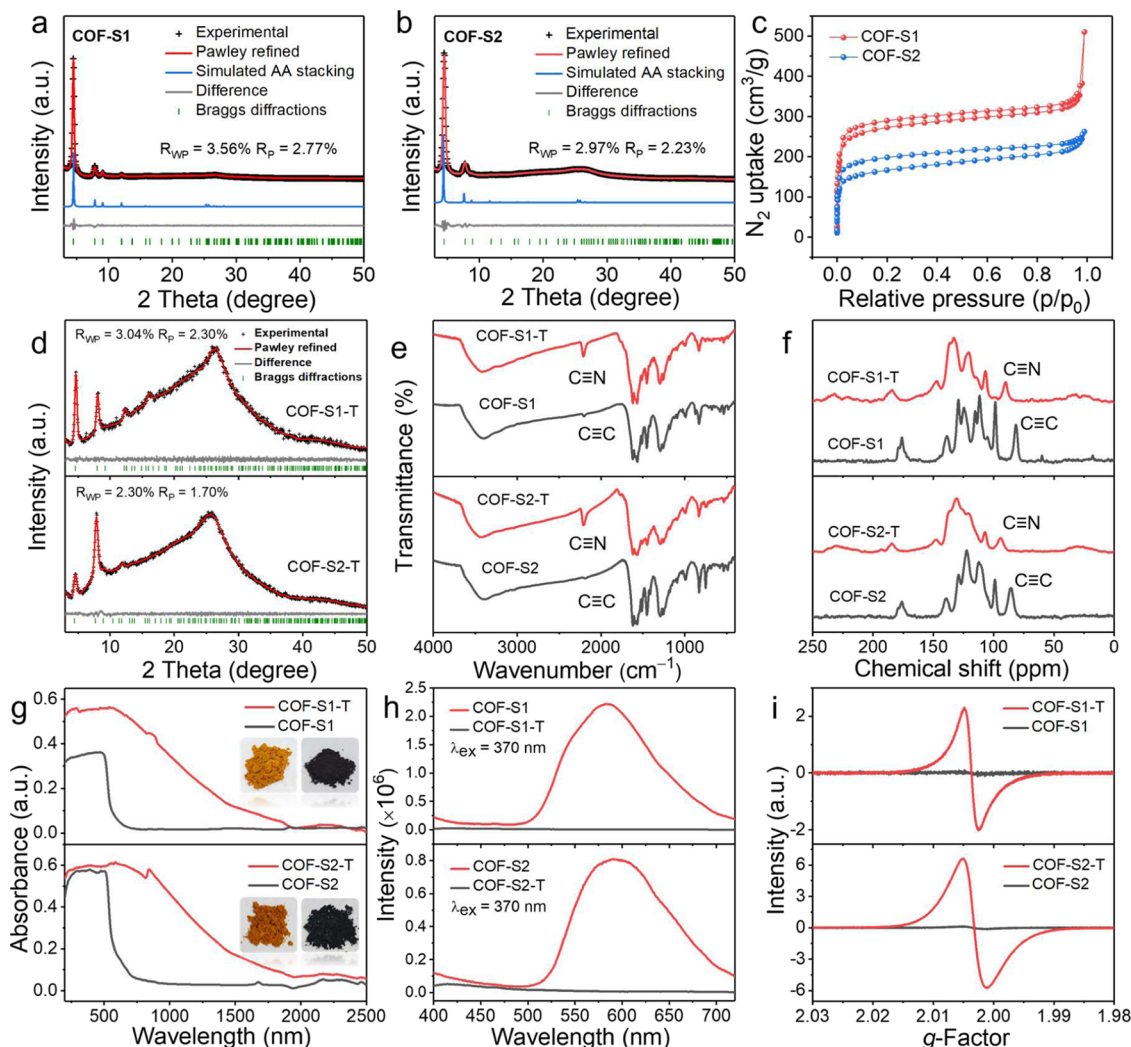
Figure 2. Experimental (plus), Pawley-refined (red), and simulated XRD patterns (AA stacking, blue) of COF−S1 (a), COF−S2 (b), and their N_2 sorption isotherms (c). (d) Experimental (plus) and Pawley-refined (red) XRD patterns for the TCNE-modified COF−S1-T and COF−S2-T. (e) FT-IR spectra, (f) ^{13}C CP/MAS NMR spectroscopic analysis, (g) UV−vis−NIR absorption spectra at room temperature, (h) photoluminescence spectra at room temperature, and (i) solid-state EPR spectra at room temperature for COF−S1, COF−S2, COF−S1-T, and COF−S2-T (1.0 mg each).

both insignificant (Figure S35), indicating pore blocking at this low temperature using the N_2 probe.

The PXRD patterns of COF−S1-T and COF−S2-T also feature a broad hump gradually sloping from low angles (*e.g.*, 5°) to peak at 26° (corresponding to the typical interlayer spacing of 3.4 Å). Such broadening suggests the loss of periodicity along the stacking direction (*i.e.*, the *c* axis), as the bulky TCBD groups formed in COF−S1-T and COF−S2-T networks can push apart the individual 2D sheets, to result in various interlayer spacings. But such broadening could also arise from some amorphous side products generated in the TCNE treatment.

To assess the likelihood of side reactions in the TCNE treatment, we similarly conducted a model reaction (Scheme S4) between TCNE and the powder sample of molecules T1−Tp, which feature the same *β*-ketoenamine units as in COF−S1 and COF−S2 solids. The reaction is less complete than the COF cases (perhaps because it is harder for TCNE to penetrate the close-packed T1−Tp solid), forming all three expected *CA-RE* products shown in Scheme S4 (see Figure S12 for the MS spectrum and Figure S13 for the solid-state ^{13}C

NMR indicating the persistence of the C≡C peak after reacting T1−Tp with TCNE—unlike the clean absence of the C≡C peak for the COF cases, as shown in Figure 2f). But solution NMR finds no other side product of the reaction with T1−Tp (Figure S14), suggesting the dominance of the *CA-RE* reaction and the stability of its products in the solid state at 140 °C.

Thermogravimetric analysis (TGA) in a N_2 atmosphere indicates that the majority of weight (weight loss <10%) in both COF−Ss and COF−Ss-T retain up to 400 °C, and afterward, the COF−Ss-T samples exhibit greater weight losses than the pristine samples of COF−Ss, which is also consistent with the weight accrued from the *CA-RE* reaction with TCNE (Figures S25 and S30).

The black color of the COF−Ss-T solids is consistent with their broad UV−vis−NIR absorption extending up to about 1900 nm (0.65 eV; Figure 2g). The electronic band gaps of COF−S1-T and COF−S2-T were determined by the Kubelka−Munk equation to be 0.95 and 0.87 eV, respectively, which are smaller than those of COF−S1 (2.17 eV) and COF−S2 (2.23 eV; Figures S43 and S44). More broadly,
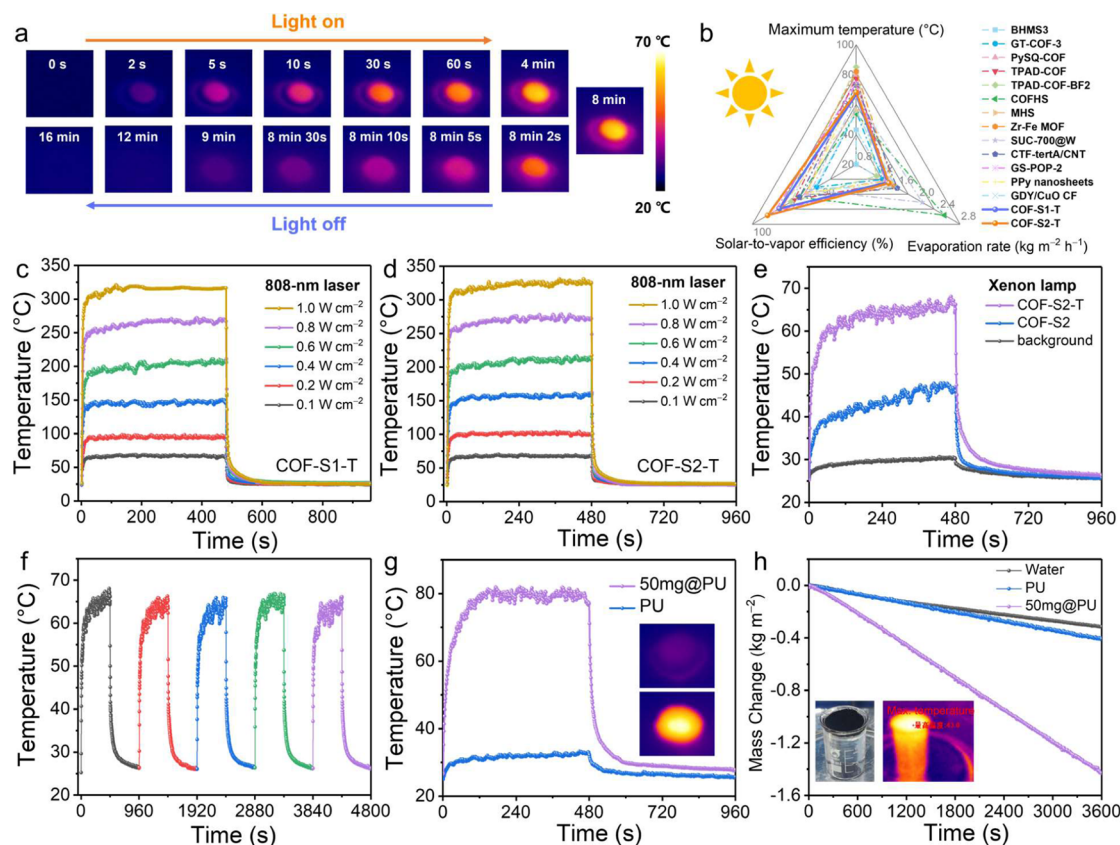
Figure 3. (a) IR thermal images of COF−S2-T powders (50 mg) under xenon lamp irradiation within 480 s and then with the xenon lamp turned off (0.1 W cm^{-2}, simulated sunlight). (b) Comparison of the performances among photothermal properties and solar water evaporators based on various materials reported in one-sun illumination. (c,d) Temperature changes of COF−S1-T and COF−S2-T powders (50 mg) under 808 nm laser irradiation at different power densities. (e) Temperature changes of COF−S2 and COF−S2-T powders (50 mg) under xenon lamp irradiation (0.1 W cm^{-2}). (f) Anti-photobleaching property of COF−S2-T powder (50 mg) during five cycles of the heating−cooling process. (g) Temperature changes of COF−S2-T@PU foam (50 mg loading of COF−S2-T) under xenon lamp irradiation (0.1 W cm^{-2}) within 480 s and then with the xenon lamp turned off. (h) Water evaporation of the blank (black), PU (blue), and COF−S2-T@PU foam (50 mg loading of COF−S2-T, purple) floating on water under one-sun light irradiation for 1 h.

COF−S1-T and COF−S2-T absorb at significantly longer wavelengths than *CA-RE*-derived molecules and materials,[71−75] exhibiting a band gap similar to that of an MOF system extensively cross-linked through the *CA-RE* modification.[24] To give more insights, COF−S1-T and COF−S2-T models with the triplet state (spins denoted as α and β) were constructed for theoretical investigation of the electronic states. The results show that the highest occupied molecular orbital−lowest unoccupied molecular orbital (HOMO−LUMO) gaps of β spin in both COF−S1-T and COF−S2-T models are 0.955 and 0.741 eV, respectively (Figure S40), consistent with those obtained electronic band gaps of COF−S1-T (0.95 eV) and COF−S2-T (0.87 eV). Importantly, in both COF−S1-T and COF−S2-T models, the HOMO (β) is dominantly on the β-ketoenamine moiety, while the LUMO (β) is mainly on the TCBD unit (Figure S40), in agreement with the proposed donor−acceptor junction and supporting the intramolecular charge transfer from the β-ketoenamine donor to the TCBD acceptor as the origin for the low-energy band gaps observed for COF−S1-T and COF−S2-T. While the orange COF−S1 and COF−S2 solids are strongly fluorescent, the black COF−S1-T and COF−S2-T are both non-emissive (as shown in Figure 2h), which is expected of the majority of TCBD derivatives formed from *CA-RE* reactions.[76,77] As strong donor−acceptor TCBD functions can give rise to open-shell,

radical species,[72,73,75] we wonder if the conjugated TCBD-based frameworks of COF−S1-T and COF−S2-T also contain unpaired electrons which may also help account for the broad near IR absorption.

Characterization of Radicals

Both COF−S1-T and COF−S2-T solids (each sample being 1.0 mg) were electron paramagnetic resonance (EPR)-active, with the signal of the larger-π and more crowded (triphenylene-based) COF−S2-T (*g*-factor = 2.0048) about three times stronger than that of COF−S1-T (*g*-factor = 2.0050; Figure 2i). By comparison, the pristine (*i.e.*, not treated by TCNE) COF−S1 and COF−S2 solids showed negligible EPR signals (Figure 2i). In another comparison, the EPR signal of the solid sample (1.0 mg) of the model molecule S1-T (Scheme S3 for the structure and Figure S6 for EPR signals) is much weaker than that of COF−S1-T. Compared with the isolated amino group in molecule S1-T, the large-π, electron-rich β-ketoenamine node can more readily donate electrons to the TCBD units to generate the EPR-active open-shell species, as is also observed in the strong EPR signals of the β-ketoenamine molecules of T1−Tp-T (made from reacting TCNE with T1−Tp, Figure S11a). For further characterization, the variable-temperature magnetic susceptibility measurement of COF−S2-T was conducted under a dc magnetic field of 1000 Oe at 2−300 K. The $\chi_M T$ versus T

plot of COF−S2-T shows that the $\chi_M T$ value is 2.936 cm^3 K mol^{-1} at 300 K and decreases to 0.024 cm^3 K mol^{-1} at 2 K (Figure S38). COF−S2-T (M_w: 1116.09 g mol^{-1}, C$_{69}$H$_{29}$N$_{15}$O$_3$) exhibits paramagnetism at 2−300 K, and the net $\chi_M T$ value of 2.912 cm^3 K mol^{-1} is contributed by the organic radicals. The experimental effective magnetic moment (μ_{eff}) was obtained as 4.83 B.M. according to $\mu_{eff} = (8\chi_M T)^{1/2}$, and the theoretical μ_{eff} is calculated to be 4.90 B.M. according to $\mu_{eff} = g[S(S + 1)]^{1/2}$ (g-factor = 2 is generally assumed), when $S = 2$ (four unpaired electrons) and $\mu_{eff} = 2[2(2 + 1)]^{1/2}$ = 4.90 B.M., which agrees well the measured value. Based on the above results, each unit (C$_{69}$H$_{29}$N$_{15}$O$_3$) in COF−S2-T carries four unpaired electrons, probably distributed over the TCBD units and β-ketoenamine nodes in COF−S2-T. The above analysis is therefore consistent with the charge transfer scheme proposed in Figure S39, but the possibility of some other charge transfer complex remains worthy of consideration in further studies.

Photothermal Performance of COF−Ss-T

Notably, COF−S1-T and COF−S2-T solids exhibit stability (unchanged PXRD patterns and FT-IR profiles) even after being heated at 300 °C for 1 h and exposed to irradiation by an 808 nm laser (Figures S48 and S55). Also, the thermal conductivities at room temperature of COF−S1-T and COF−S2-T were found to be 0.10 and 0.35 W K^{-1} m^{-1}, respectively (Figure S42), indicative of their thermally insulative features. Because of the broad absorption profile and thermal stability in air, the COF−S1-T and COF−S2-T solids were tested for photothermal conversion applications. The temperature changes of each powder (50 mg) upon irradiation by an 808 nm laser were first recorded by an infrared camera to evaluate the photothermal conversion performance. The COF−S2-T powder rapidly increased from 25 to 309 °C within 20 s under 808 nm laser irradiation (1.0 W cm^{-2}) and maintained a high temperature at about 331 °C for the next 8 min (Figures 3d and S53). After the removal of the laser, the temperature dropped rapidly to room temperature. Compared to the COF−S1-T powder (Figure 3c), the maximum temperature of the COF−S2-T powder was about 11 °C higher under the same experimental conditions: its more efficient photothermal conversion is consistent with its larger-π, triphenylene system and its higher density of radicals (as per the EPR spectra). In addition, the maximum stable temperature of COF−Ss-T gradually increased with elevating power density in a linear relationship (Figure S54). Compared with the reported network of GT−COF−3 (absorption up to 1400 nm), which features the TCBD units as side chains,[75] the COF−Ss-T systems integrate the TCBD units into the backbone for conjugation with the strongly electron-donating β-ketoenamine nodes and achieve broader light absorption profiles (e.g., absorption up to 1900 nm) and better photothermal properties.

Under one-sun irradiation (420−2500 nm) simulated with a xenon lamp (0.1 W cm^{-2}), the COF−Ss-T powders also exhibited efficient solar-thermal conversion. Specifically, after 8 min, COF−S2-T (50 mg) registers a maximum temperature of 68 °C (Figures 3a and 3e; 66.7 °C for COF−S1-T, Figures S59 and S60)—one of the highest values reached under this irradiation condition (Figure 3b and Table S17), while the pristine COF−S2 did not exceed 50 °C under the same conditions. In addition, the framework solids of COF−S1-T and COF−S2-T offer advantages in stability (e.g., not to be

washed away by solvents) and porosity. The porosity also allows the TCNE molecules to fully access and convert the alkyne units, compared with the incomplete reaction between TCNE and the molecular solid of T1−Tp (cf. Figures 2c, S16, and S18). The COF−Ss-T powders are also found to be resistant to photobleaching: the maximum temperatures remained the same after five cycles of xenon lamp on−off irradiation (Figures 3f and S61), and the IR and PXRD features were also not changed, demonstrating the photothermal stability of COF−Ss-T (Figure S62).

Photothermal conversion for water evaporation/purification (e.g., for sewage treatment) is a growing technology for utilizing solar energy. As shown in Figures 1c and S46, the CA-RE modification increases hydrophilicity, e.g., with the water contact angle changing from 75° (COF−S2) to 34° (COF−S2-T); due to its many strong donors of polar cyano groups hydrogen-bonding with water), which is suited for water evaporation use. The solar water evaporation system was constructed by loading the COF−Ss-T powders on polyurethane (PU) foams. Porous PU foams offer good thermal insulation and water transport,[75,78] thus suitable for being floating carriers of COF−Ss-T powders to assist interfacial water evaporation. Specifically, 10−50 mg of COF−Ss-T powders were loaded on PU films with a diameter of 2.2 cm to afford a series of black COF−Ss-T@PU foams (Figures S64 and S65). The photothermal conversion behaviors of the COF−Ss-T@PU foams were then evaluated by using the same method as for the COF powders. In comparison to the COF−Ss-T powders, COF−Ss-T@PU foams (50 mg) reach a higher stable temperature of 80 °C under one-sun irradiation (Figures 3g and S66). Therefore, COF−Ss-T@PU foams were tested for solar water evaporation, and the water evaporation rate increases with higher COF loading (with up to 50 mg of COF−Ss-T powders loaded on the PU film; Figures S68 and S69). The changes in temperature and mass within 1 h under the simulated solar irradiation were recorded, and the water evaporation interface temperature of COF−S2-T@PU foam (50 mg) can reach 43.3 °C (Figure S69). The solar-driven water evaporation efficiency was calculated to be 97.8%, which was much higher than that of pure PU foam (i.e., 30.5%; Figure 3h and Table S7). Additionally, the COF−Ss-T powders were found to be chemically stable (by stirring for one day) in water at 100 °C and in aqueous solutions of pH = 5, 7, and 9 at room temperature (Figure S45). Thus, COF−Ss-T@PU foams can be used for pure water evaporation, as well as sewage treatment or seawater desalination under real-life conditions. By comparison, carbon materials (e.g., activated carbon and carbon black) also have a wide visible light absorption range (200−2500 nm for activated carbon) for capturing photons,[79,80] but their hydrophobicity limits the use for solar water evaporation, not to mention the safety issues associated with their electrical conductivity. Therefore, the hydrophilic and electrically insulating COF−Ss-T powders offer clear advantages over carbon materials, including the higher evaporation efficiency (in part enabled by the hydrophilicity; Figure S71).

Solar Thermoelectric Generation

The heat converted from sunlight can also be turned into electricity by means of a solar thermoelectric generator (STEG), which represents a promising clean energy technology.[81,82] According to the Seebeck effect, to generate strong voltage, it is key to increase the temperature difference between the two ends of a thermoelectric device. As shown in
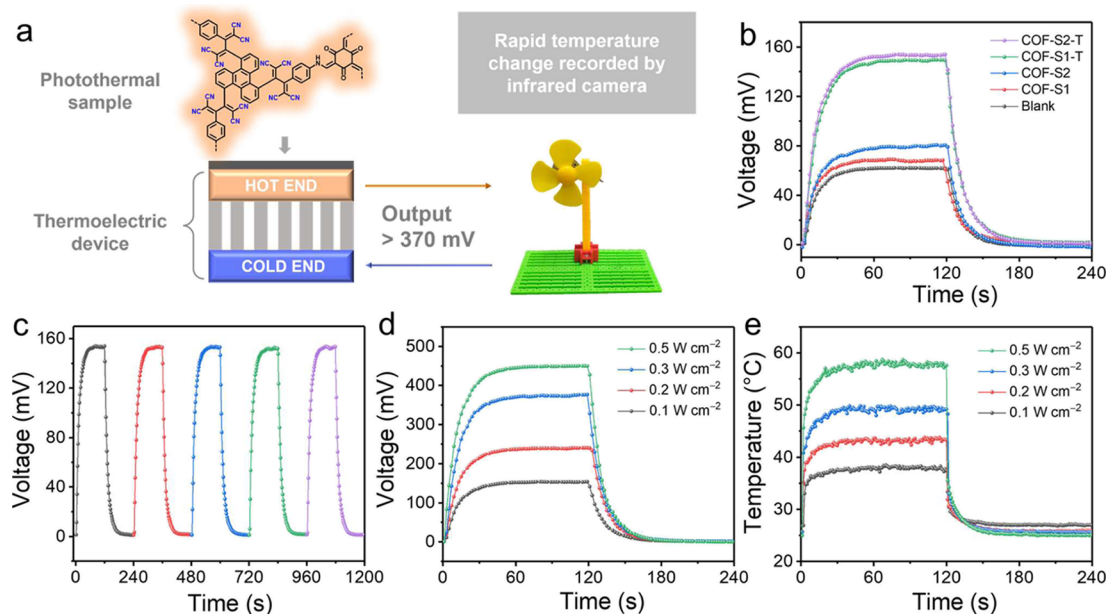
Figure 4. (a) Design of the thermoelectric device to power a fan. (b) Voltage changes of COF-Ss and COF-Ss-T powder (50 mg) upon xenon lamp irradiation at 0.1 W cm^{-2} within 120 s and then with the xenon lamp turned off. (c) Voltage changes of COF−S2-T powder (50 mg, xenon lamp irradiation at 0.1 W cm^{-2}) during five cycles of the heating-cooling process. (d) Voltage and (e) upper surface temperature changes of COF−S2-T powder (50 mg) coated onto the surface of the thermoelectric device under xenon lamp irradiation at different laser powers (0.1, 0.2, 0.3, and 0.5 W cm^{-2}) within 120 s and then with the xenon lamp turned off.
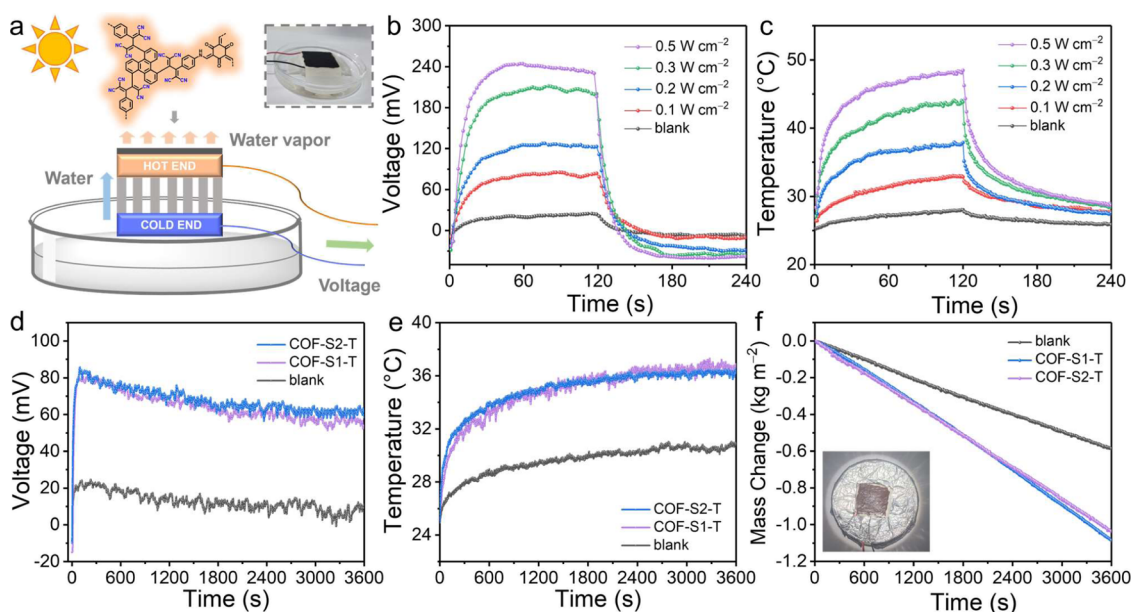

Figure 5. (a) Diagram of the solar-water evaporation-thermoelectric generator device for water evaporation and thermoelectric generation. The inset shows the actual device. (b) Voltage and (c) upper surface temperature changes of COF−S2-T powder (50 mg) attached to the filter paper on the surface of the thermoelectric device under xenon lamp irradiation at different laser powers within 120 s and then with the xenon lamp turned off. (d) Voltage changes, (e) upper surface temperature changes, and (f) water evaporation of blank (black), COF−S1-T (purple), and COF−S2-T (blue) powder (50 mg) attached to the filter paper on the surface of the thermoelectric device under xenon lamp irradiation of 0.1 W cm^{-2} for 1 h. The inset shows the actual device.

Figures 4a and S72, using a xenon lamp as the light source, the photothermal−electric conversion device was constructed by coating various amounts of COF−Ss-T powder on the surface of the hot end, with the surface of the cold end connected to a condensation device. Upon xenon lamp irradiation, the resulting temperature gradient between the hot and cold ends produces a voltage difference. The voltage can be recorded by a multimeter, and the temperature, by an infrared camera. The thermoelectric device loaded with COF−Ss-T powders at the hot end showed a larger temperature difference and higher voltage than the blank sample (Figure 4b). Under xenon lamp irradiation (0.1 W cm^{-2}), the hot-end temperature increased with higher COF−Ss-T loading, but the voltage did not change but decreased instead (Figures S80 and S86). This

can be attributed to the low density of the COF powders. As the thickness of COF layer increases with higher loading, the actual temperature difference between the hot and cold ends becomes smaller. To fully cover the surface of the thermoelectric device by the COF−Ss-T powder, a loading of 50 mg was selected for the following experiments. The thermoelectric device remained stable after five cycles of xenon lamp on−off irradiation (0.1 W cm^{-2}), highlighting the stability of the photothermal-to-electric conversion device (Figures 4c and S82). Furthermore, the thermoelectric performance of the device irradiated at different power densities was investigated. The final stable voltage output of the thermoelectric device loaded with COF−Ss-T (50 mg) increases with elevating xenon lamp intensity (Figures 4d−e and S83 and S84). To visualize the photothermal-to-electric conversion, the thermoelectric devices were used to power an electric fan. When the power density of the light source reaches 0.3 W cm^{-2}, the voltage output of 370 mV can start the fan (Figure S92), and the fan stops immediately when the light source is removed, highlighting the swift response of electricity generation to light. Our materials thus compare favorably with many organic phase change materials (PCMs; e.g., n-octadecane), as these are often poor light absorbers and need additives of high thermal conductivity and photon absorption (e.g., boron nitride and graphene) for STEG assembly.[83−88] Moreover, STEG devices using composite phase change materials generally require longer (minutes or even hours) irradiation time to affect the phase change and thermal energy conversion.

Low-grade waste heat generated by photothermal materials during water evaporation can be applied to thermoelectric conversion in order to construct a simple solar-water evaporation-thermoelectric generator device (Figure S93). By loading the photothermal materials on the hot end of the thermoelectric device as a solar collector, the generated heat is not only transferred to the interface for water evaporation but also forms a temperature difference with the cold end for voltage generation, thereby simultaneously realizing water evaporation and thermoelectric conversion. The device was improved by adding a filter paper for transporting water to ensure the stability of interfacial water evaporation, while maintaining thermoelectric conversion (Figures 5a and S94). Thus, the multifunctional device with COF-Ss-T powder (50 mg loading) gave a continuous voltage output (Figure 5d) and solar-water evaporation efficiency of more than 70% under 0.1 W cm^{-2} xenon lamp irradiation (Figure 5e−f). The generated voltage increases with stronger irradiation (Figures 5b−c and Figure S97), and it is generally 3.5 times higher than the corresponding value of the blank sample, and it can exceed half of the above single-purpose thermoelectric device. The implementation of such a simple, multifunctional solar-water evaporation-thermoelectric generator highlights the versatility of our photothermal materials in the clean and efficient utilization of solar energy.

CONCLUSIONS

In conclusion, our effort to boost the clean use of solar energy has motivated us to leverage our skills across organic chemistry and crystal engineering to develop highly efficient photothermal materials, as is showcased in the organic framework solids of COF−S1-T and COF−S2-T. Our design invoked the strongly light absorbing push−pull TCBD units that have been established in solution chemistry (i.e., via the CA-RE reaction), and our design has also greatly benefited from the stable and

functional β-ketoenamine-based framework system developed by other pioneers in the field. By uniting the CA-RE reaction and β-ketoenamine framework, we have made two surprising discoveries: (1) the surprising framework flexibility/reactivity: who would have thought that the elaborate and bulky TCBD units can be so readily generated from the alkyne units imbedded in the stacked 2D networks! (2) the surprising density of radical species, which, in hindsight, can be rationalized by the β-ketoenamine donors and TCBD acceptors integrated within the conjugated structures. We hope that our work would not only attract more attention to radical-based photoactive materials but also spur more studies on the flexibility and reactivity of framework materials, in order to broaden the functionalities in the solid state.

METHODS

Synthesis of COF−S1

S1 (20 mg, 48 μmol) and Tp (10 mg, 48 μmol) were dispersed into a glass tube (8 × 150 mm) charged with the solution of 0.50 mL of mesitylene/0.50 mL of 1,4-dioxane/0.1 mL of 6 M aqueous acetic acid/13 μL of aniline. The mixture was sonicated for 10 min to form a homogeneous dispersion. The reaction mixture was heated at 120 °C for 3 days under a static condition. After cooling, the precipitate was collected by filtration and washed with DMF and THF and subjected to Soxhlet extraction with THF for 3 days. The orange powder was collected and dried at 120 °C under vacuum overnight to give COF−S1. (Yield: 83%).

Synthesis of COF−S2

S2 (22 mg, 38 μmol) and Tp (8 mg, 38 μmol) were dispersed into a glass tube (8 × 150 mm) charged with the solution of 0.50 mL of mesitylene/0.50 mL of 1,4-dioxane/0.1 mL of 6 M aqueous acetic acid/10 μL of aniline. The mixture was sonicated for 10 min to form a homogeneous dispersion. The reaction mixture was heated at 120 °C for 3 days under a static condition. After cooling, the precipitate was collected by filtration and washed with DMF and THF and subjected to Soxhlet extraction with THF for 3 days. The orange red powder was collected and dried at 120 °C under vacuum overnight to give COF−S2. (Yield: 78%).

Synthesis of COF−S1-T

COF−S1 (50 mg) and TCNE (50 mg, 0.39 mol) were placed in a 25 mL Schlenk tube, with spatial separation maintained to prevent the two from directly contacting each other (e.g., by holding TCNE in a smaller tube sealed at one end). After the air was evacuated from the Schlenk tube, the tube was placed in an oven preheated to 140 °C to promote sublimation/vapor transport of TCNE. A new batch of TCNE powder was substituted every 24 h for two times. After 72 h, the tube was removed from the oven to cool down to room temperature. The obtained powder was washed with DMF and THF and subjected to Soxhlet extraction with THF for 3 days and dried in vacuo at 100 °C (5 h) to afford the brownish black powder, COF−S1-T.

Synthesis of COF−S2-T

The synthesis was carried out following the synthetic procedure of COF−S1-T using COF−S2 in place of COF−S1, and COF−S2-T was obtained as black powders.

Photothermal Conversion Measurement

Photothermal measurements of COF−Ss-T powder (50 mg) were performed by using an 808 nm laser (FLMM-0808, Xi'an Herschel Laser Technology Co. Ltd., China) and the xenon lamp (AM 1.5 G, PLS-SXE300+). The temperature response of the samples was measured with an IR thermal camera (MAG14, Shanghai Magnity Technologies Co. Ltd., China).

Fabrication of COF-Loaded PU Foams

10−50 mg of COF samples was ground carefully and then ultrasonically dispersed in 2 mL of ethanol and 200 μL of 5% Nafion. The COF-loaded polyurethane (PU) foams were obtained by dropping the resulting suspensions onto circular and porous PU foams with diameters of 2.2 cm and drying under 70 °C under vacuum for 1 h.

Solar-Driven Vapor Generation Experiments

The COF-loaded PU foams were allowed to float on water in a quartz beaker (see Figure S56). Sunlight was simulated by a xenon lamp (PLS-SXE300+) with an optical filter (AM 1.5 G) and used to irradiate the sample under specific power density. The mass change of the water was recorded by an electronic balance (accuracy of 0.1 mg). An IR camera was used to measure the temperature.

■ ASSOCIATED CONTENT

ⓈⒾ Supporting Information

The Supporting Information is available free of charge at https://pubs.acs.org/doi/10.1021/jacsau.3c00132.

> Experimental details, ^1H, ^{13}C, and ^{13}C CP/MAS NMR spectra, ESI-MS spectra, FT-IR spectra, PXRD patterns, structure refinement details, TGA spectra, XPS spectra, gas sorption profiles, SEM images, TEM images, magnetic susceptibility plots, thermal conductivity plots, UV−vis DRS spectra, HOMO−LUMO plots of COF models, water contact angle data, photothermal conversion and solar-driven water evaporation data set, elemental analysis results, BET surface area, solar-driven water evaporation capability, thermoelectric conversion capability, atomic coordinates, photothermal properties, and performance metrics (PDF)

■ AUTHOR INFORMATION

Corresponding Authors

Lai-Hon Chung − *School of Chemical Engineering and Light Industry, Guangdong University of Technology, Guangzhou 510006, China;* ⓞ orcid.org/0000-0002-0482-1362; Email: laihonchung@gdut.edu.cn

Zhengtao Xu − *Institute of Materials Research and Engineering (IMRE), Agency for Science, Technology and Research (A*STAR), Singapore 138634, Singapore;* ⓞ orcid.org/0000-0002-7408-4951; Email: zhengtao@imre.a-star.edu.sg

Jun He − *School of Chemical Engineering and Light Industry, Guangdong University of Technology, Guangzhou 510006, China;* ⓞ orcid.org/0000-0001-7062-4001; Email: junhe@gdut.edu.cn

Authors

Zhiqing Lin − *School of Chemical Engineering and Light Industry, Guangdong University of Technology, Guangzhou 510006, China*

Yuan-Hui Zhong − *School of Chemical Engineering and Light Industry, Guangdong University of Technology, Guangzhou 510006, China*

Leheng Zhong − *School of Chemical Engineering and Light Industry, Guangdong University of Technology, Guangzhou 510006, China*

Xinhe Ye − *School of Chemical Engineering and Light Industry, Guangdong University of Technology, Guangzhou 510006, China*

Xuanhe Hu − *School of Chemical Engineering and Light Industry, Guangdong University of Technology, Guangzhou 510006, China;* ⓞ orcid.org/0000-0003-1779-2617

Lin Yu − *School of Chemical Engineering and Light Industry, Guangdong University of Technology, Guangzhou 510006, China;* ⓞ orcid.org/0000-0001-6187-6514

Complete contact information is available at:
https://pubs.acs.org/10.1021/jacsau.3c00132

Author Contributions

Credit: Z.L., L.-H.C., Z.X., and J.H. conceived and designed the experiments. Z.L. and L.Z. synthesized the materials. L.Z. and Y.-H.Z. analyzed the COF structure. Y.-H.Z. performed the theoretical calculation and analyzed the data. L.-H.C. and X.Y. analyzed the EPR and magnetic data. Z.L., L.Z., X.Y., Y.-H.Z., L.-H.C., X.H., Z.X., L.Y., and J.H. analyzed the data and co-wrote the manuscript. All authors discussed the results and commented on the manuscript. CRediT: **Zhiqing Lin** data curation, investigation, methodology, writing-original draft; **Yuan-Hui Zhong** software, validation, visualization; **Leheng Zhong** data curation, formal analysis; **Xinhe Ye** formal analysis, methodology; **Lai-Hon Chung** conceptualization, formal analysis, visualization, writing-original draft, writing-review & editing; **Xuanhe Hu** formal analysis, validation; **Zhengtao Xu** conceptualization, supervision, writing-original draft, writing-review & editing; **Lin Yu** resources, writing-review & editing; **Jun He** conceptualization, funding acquisition, supervision, writing-review & editing.

Notes

The authors declare no competing financial interest.

■ ACKNOWLEDGMENTS

■ REFERENCES

(1) Deria, P.; Mondloch, J. E.; Karagiaridi, O.; Bury, W.; Hupp, J. T.; Farha, O. K. Beyond post-synthesis modification: evolution of metal-organic frameworks via building block replacement. *Chem. Soc. Rev.* **2014**, *43*, 5896−5912.

(2) Segura, J. L.; Royuela, S.; Mar Ramos, M. Post-synthetic modification of covalent organic frameworks. *Chem. Soc. Rev.* **2019**, *48*, 3903−3945.

(3) Yan, Q.; Xu, H.; Jing, X.; Hu, H.; Wang, S.; Zeng, C.; Gao, Y. Post-synthetic modification of imine linkages of a covalent organic framework for its catalysis application. *RSC Adv.* **2020**, *10*, 17396−17403.

(4) Ding, H.; Mal, A.; Wang, C. Tailored covalent organic frameworks by post-synthetic modification. *Mater. Chem. Front.* **2020**, *4*, 113−127.

(5) Cusin, L.; Peng, H.; Ciesielski, A.; Samori, P. Chemical Conversion and Locking of the Imine Linkage: Enhancing the

Functionality of Covalent Organic Frameworks. *Angew. Chem., Int. Ed.* **2021**, *60*, 14236−14250.

(6) Bhadra, B. N.; Ahmed, I.; Lee, H. J.; Jhung, S. H. Metal-organic frameworks bearing free carboxylic acids: Preparation, modification, and applications. *Coord. Chem. Rev.* **2022**, *450*, 214237.

(7) Xu, Z.; Lee, S.; Kiang, Y. H.; Mallik, A. B.; Tsomaia, N.; Mueller, K. T. A Cross-linked Large Channel Organic Coordination Solid. *Adv. Mater.* **2001**, *13*, 637−641.

(8) Guo, Z.; Zhang, Y.; Dong, Y.; Li, J.; Li, S.; Shao, P.; Feng, X.; Wang, B. Fast Ion Transport Pathway Provided by Polyethylene Glycol Confined in Covalent Organic Frameworks. *J. Am. Chem. Soc.* **2019**, *141*, 1923−1927.

(9) Begum, S.; Hassan, Z.; Brase, S.; Tsotsalas, M. Polymerization in MOF-Confined Nanospaces: Tailored Architectures, Functions, and Applications. *Langmuir* **2020**, *36*, 10657−10673.

(10) Jadhav, T.; Fang, Y.; Liu, C. H.; Dadvand, A.; Hamzehpoor, E.; Patterson, W.; Jonderian, A.; Stein, R. S.; Perepichka, D. F. Transformation between 2D and 3D Covalent Organic Frameworks via Reversible [2 + 2] Cycloaddition. *J. Am. Chem. Soc.* **2020**, *142*, 8862−8870.

(11) Li, Z.; He, T.; Gong, Y.; Jiang, D. Covalent Organic Frameworks: Pore Design and Interface Engineering. *Acc. Chem. Res.* **2020**, *53*, 1672−1685.

(12) Kong, F. X.; Yue, L.; Yang, Z.; Sun, G.; Chen, J. F. Cross-Linked Covalent Organic Framework-Based Membranes with Trimesoyl Chloride for Enhanced Desalination. *ACS Appl. Mater. Interfaces* **2021**, *13*, 21379−21389.

(13) Kuehl, V. A.; Duong, P. H. H.; Sadrieva, D.; Amin, S. A.; She, Y.; Li-Oakey, K. D.; Yarger, J. L.; Parkinson, B. A.; Hoberg, J. O. Synthesis, Postsynthetic Modifications, and Applications of the First Quinoxaline-Based Covalent Organic Framework. *ACS Appl. Mater. Interfaces* **2021**, *13*, 37494−37499.

(14) Li, M.-Q.; Wong, Y.-L.; Lum, T.-S.; Sze-Yin Leung, K.; Lam, P. K. S.; Xu, Z. Dense thiol arrays for metal−organic frameworks: boiling water stability, Hg removal beyond 2 ppb and facile crosslinking. *J. Mater. Chem. A* **2018**, *6*, 14566−14570.

(15) Liu, D. C.; Ouyang, T.; Xiao, R.; Liu, W. J.; Zhong, D. C.; Xu, Z.; Lu, T. B. Anchoring Co(II) Ions into a Thiol-Laced Metal-Organic Framework for Efficient Visible-Light-Driven Conversion of CO_2 into CO. *ChemSusChem* **2019**, *12*, 2166−2170.

(16) Wong, Y. L.; Diao, Y.; He, J.; Zeller, M.; Xu, Z. A Thiol-Functionalized UiO-67-Type Porous Single Crystal: Filling in the Synthetic Gap. *Inorg. Chem.* **2019**, *58*, 1462−1468.

(17) Yang, Q.; Guo, Y.; Yan, B.; Wang, C.; Liu, Z.; Huang, Z.; Wang, Y.; Li, Y.; Li, H.; Song, L.; Fan, J.; Zhi, C. Hydrogen-Substituted Graphdiyne Ion Tunnels Directing Concentration Redistribution for Commercial-Grade Dendrite-Free Zinc Anodes. *Adv. Mater.* **2020**, *32*, No. e2001755.

(18) Zhou, H. Q.; He, Y.; Hu, J. Y.; Chung, L. H.; Gu, Q.; Liao, W. M.; Zeller, M.; Xu, Z.; He, J. Conjugated crosslinks boost the conductivity and stability of a single crystalline metal-organic framework. *Chem. Commun.* **2021**, *57*, 187−190.

(19) He, Y.; Dong, J.; Liu, Z.; Li, M. Q.; Hu, J.; Zhou, Y.; Xu, Z.; He, J. Dense Dithiolene Units on Metal-Organic Frameworks for Mercury Removal and Superprotonic Conduction. *ACS Appl. Mater. Interfaces* **2022**, *14*, 1070−1076.

(20) Hou, Y. L.; Li, M. Q.; Cheng, S.; Diao, Y.; Vilela, F.; He, Y.; He, J.; Xu, Z. Dramatic improvement of stability by in situ linker cyclization of a metal-organic framework. *Chem. Commun.* **2018**, *54*, 9470−9473.

(21) Qin, J. S.; Yuan, S.; Zhang, L.; Li, B.; Du, D. Y.; Huang, N.; Guan, W.; Drake, H. F.; Pang, J.; Lan, Y. Q.; Alsalme, A.; Zhou, H. C. Creating Well-Defined Hexabenzocoronene in Zirconium Metal-Organic Framework by Postsynthetic Annulation. *J. Am. Chem. Soc.* **2019**, *141*, 2054−2060.

(22) Diao, Y.; Hu, J.; Cheng, S.; Ma, F.; Li, M. Q.; Hu, X.; Li, Y. Y.; He, J.; Xu, Z. Dense Alkyne Arrays of a Zr(IV) Metal-Organic Framework Absorb $Co_2(CO)_8$ for Functionalization. *Inorg. Chem.* **2020**, *59*, 5626−5631.

(23) Cheng, S.; Tieu, P.; Gao, W.; Hu, J.; Feng, W.; He, J.; Pan, X.; Xu, Z. Crystallinity after decarboxylation of a metal-carboxylate framework: indestructible porosity for catalysis. *Dalton Trans.* **2020**, *49*, 11902−11910.

(24) Cheng, S.; Li, K.; Hu, J.; He, J.; Zeller, M.; Xu, Z. Building Conjugated Donor-Acceptor Cross-Links into Metal-Organic Frameworks for Photo- and Electroactivity. *ACS Appl. Mater. Interfaces* **2020**, *12*, 19201−19209.

(25) Frahm, D.; Hoffmann, F.; Fröba, M. Two Metal−Organic Frameworks with a Tetratopic Linker: Solvent-Dependent Polymorphism and Postsynthetic Bromination. *Cryst. Growth Des.* **2014**, *14*, 1719−1725.

(26) Marshall, R. J.; Griffin, S. L.; Wilson, C.; Forgan, R. S. Single-Crystal to Single-Crystal Mechanical Contraction of Metal-Organic Frameworks through Stereoselective Postsynthetic Bromination. *J. Am. Chem. Soc.* **2015**, *137*, 9527−9530.

(27) Marshall, R. J.; Richards, T.; Hobday, C. L.; Murphie, C. F.; Wilson, C.; Moggach, S. A.; Bennett, T. D.; Forgan, R. S. Postsynthetic bromination of UiO-66 analogues: altering linker flexibility and mechanical compliance. *Dalton Trans.* **2016**, *45*, 4132−4135.

(28) Moneypenny, T. P., 2nd; Walter, N. P.; Cai, Z.; Miao, Y. R.; Gray, D. L.; Hinman, J. J.; Lee, S.; Zhang, Y.; Moore, J. S. Impact of Shape Persistence on the Porosity of Molecular Cages. *J. Am. Chem. Soc.* **2017**, *139*, 3259−3264.

(29) Xu, X.; Yang, F.; Han, H.; Xu, Y.; Wei, W. Postsynthetic Addition of Ligand Struts in Metal-Organic Frameworks: Effect of Syn/Anti Addition on Framework Structures with Distinct Topologies. *Inorg. Chem.* **2018**, *57*, 2369−2372.

(30) Walshe, C. A.; Thom, A. J. R.; Wilson, C.; Ling, S.; Forgan, R. S. Controlling the Flexibility of MIL-88A(Sc) Through Synthetic Optimisation and Postsynthetic Halogenation. *Chem. Eur. J.* **2022**, *28*, No. e202201364.

(31) Jones, S. C.; Bauer, C. A. Diastereoselective Heterogeneous Bromination of Stilbene in a Porous Metal−Organic Framework. *J. Am. Chem. Soc.* **2009**, *131*, 12516−12517.

(32) Xu, Y.; Smith, M. D.; Krause, J. A.; Shimizu, L. S. Control of the Intramolecular [2+2] Photocycloaddition in a Bis-Stilbene Macrocycle. *J. Org. Chem.* **2009**, *74*, 4874−4877.

(33) Xu, Y.; Smith, M. D.; Geer, M. F.; Pellechia, P. J.; Brown, J. C.; Wibowo, A. C.; Shimizu, L. S. Thermal Reaction of a Columnar Assembled Diacetylene Macrocycle. *J. Am. Chem. Soc.* **2010**, *132*, 5334−5335.

(34) Mir, M. H.; Koh, L. L.; Tan, G. K.; Vittal, J. J. Single-crystal to single-crystal photochemical structural transformations of inter-penetrated 3 D coordination polymers by [2+2] cycloaddition reactions. *Angew. Chem., Int. Ed.* **2010**, *49*, 390−393.

(35) Medishetty, R.; Koh, L. L.; Kole, G. K.; Vittal, J. J. Solid-state structural transformations from 2D interdigitated layers to 3D interpenetrated structures. *Angew. Chem., Int. Ed.* **2011**, *50*, 10949−10952.

(36) Medishetty, R.; Husain, A.; Bai, Z.; Runcevski, T.; Dinnebier, R. E.; Naumov, P.; Vittal, J. J. Single crystals popping under UV light: a photosalient effect triggered by a [2+2] cycloaddition reaction. *Angew. Chem., Int. Ed.* **2014**, *53*, 5907−5911.

(37) Dawn, S.; Salpage, S. R.; Koscher, B. A.; Bick, A.; Wibowo, A. C.; Pellechia, P. J.; Shimizu, L. S. Applications of a bis-urea phenylethynylene self-assembled nanoreactor for [2 + 2] photo-dimerizations. *J. Phys. Chem. A* **2014**, *118*, 10563−10574.

(38) Park, I. H.; Lee, E.; Lee, S. S.; Vittal, J. J. Chemical Patterning in Single Crystals of Metal-Organic Frameworks by [2+2] Cyclo-addition Reaction. *Angew. Chem., Int. Ed.* **2019**, *58*, 14860−14864.

(39) Hema, K.; Ravi, A.; Raju, C.; Sureshan, K. M. Polymers with advanced structural and supramolecular features synthesized through topochemical polymerization. *Chem. Sci.* **2021**, *12*, 5361−5380.

(40) Hossain, M. M.; Olamilekan, A. I.; Jeong, H.-O.; Lim, H.; Kim, Y.-K.; Cho, H.; Jeong, H. D.; Islam, M. A.; Goh, M.; You, N.-H.; Kim, M. J.; Choi, S. Q.; Hahn, J. R.; Yeo, H.; Jang, S. G. Diacetylene-Containing Dual-Functional Liquid Crystal Epoxy Resin: Strategic

Phase Control for Topochemical Polymerization of Diacetylenes and Thermal Conductivity Enhancement. *Macromolecules* **2022**, *55*, 4402−4410.

(41) Lacy, A. R.; Vogt, A.; Boudon, C.; Gisselbrecht, J.-P.; Schweizer, W. B.; Diederich, F. Post-Cycloaddition-Retroelectrocyclization Transformations of Polycyanobutadienes. *Eur. J. Org. Chem.* **2013**, *2013*, 869−879.

(42) Michinobu, T.; Diederich, F. The [2+2] Cycloaddition-Retroelectrocyclization (CA-RE) Click Reaction: Facile Access to Molecular and Polymeric Push-Pull Chromophores. *Angew. Chem., Int. Ed.* **2018**, *57*, 3552−3577.

(43) Kandambeth, S.; Dey, K.; Banerjee, R. Covalent Organic Frameworks: Chemistry beyond the Structure. *J. Am. Chem. Soc.* **2019**, *141*, 1807−1822.

(44) Yuan, S.; Li, X.; Zhu, J.; Zhang, G.; Van Puyvelde, P.; Van der Bruggen, B. Covalent organic frameworks for membrane separation. *Chem. Soc. Rev.* **2019**, *48*, 2665−2681.

(45) Chen, X.; Geng, K.; Liu, R.; Tan, K. T.; Gong, Y.; Li, Z.; Tao, S.; Jiang, Q.; Jiang, D. Covalent Organic Frameworks: Chemical Approaches to Designer Structures and Built-In Functions. *Angew. Chem., Int. Ed.* **2020**, *59*, 5050−5091.

(46) Liu, L.; Yin, L.; Cheng, D.; Zhao, S.; Zang, H. Y.; Zhang, N.; Zhu, G. Surface-Mediated Construction of an Ultrathin Free-Standing Covalent Organic Framework Membrane for Efficient Proton Conduction. *Angew. Chem., Int. Ed.* **2021**, *60*, 14875−14880.

(47) Lu, Z.; Yang, C.; He, L.; Hong, J.; Huang, C.; Wu, T.; Wang, X.; Wu, Z.; Liu, X.; Miao, Z.; Zeng, B.; Xu, Y.; Yuan, C.; Dai, L. Asymmetric Hydrophosphonylation of Imines to Construct Highly Stable Covalent Organic Frameworks with Efficient Intrinsic Proton Conductivity. *J. Am. Chem. Soc.* **2022**, *144*, 9624−9633.

(48) Mu, Z.; Zhu, Y.; Li, B.; Dong, A.; Wang, B.; Feng, X. Covalent Organic Frameworks with Record Pore Apertures. *J. Am. Chem. Soc.* **2022**, *144*, 5145−5154.

(49) Bruce, M. I.; Rodgers, J. R.; Snow, M. R.; Swincer, A. G. Cyclopentadienyl -ruthenium and -osmium chemistry. Cleavage of Tetracyanoethylene under Mild Conditions: X-Ray Crystal Structures of [Ru{η³-C(CN)₂CPhC=C(CN)₂}(PPh₃)(η-C₅H₅)] and [Ru{C-[=C(CN)₂]CPh=C(CN)₂}-(CNBuᵗ)(PPh₃)(η-C₅H₅)]. *J. Chem. Soc., Chem. Commun.* **1981**, 271−272.

(50) Onitsuka, K.; Takahashi, S. Synthesis and Structure of s-*cis*- and s-*trans*-μ-Butadiene-2,3-diyldiplatinum Complexes by the Reaction of μ-Ethynediyldiplatinum Complexes with Tetracyanoethylene. *J. Chem. Soc., Chem. Commun.* **1995**, 2095−2096.

(51) Bruce, M. I.; Low, P. J.; Skelton, B. W.; White, A. H. Reaction of with tetracyanoethene: {Ru(PPh₃)₂Cp}₂(μ-C₄) macrocycle formation by intermolecular CN coordination. *New J. Chem.* **1998**, *22*, 419−422.

(52) Wu, X.; Wu, J.; Liu, Y.; Jen, A. K. Y. Highly Efficient, Thermally and Chemically Stable Second Order Nonlinear Optical Chromophores Containing a 2-Phenyl-tetracyanobutadienyl Acceptor. *J. Am. Chem. Soc.* **1998**, *121*, 472−473.

(53) Morioka, Y.; Yoshizawa, N.; Nishida, J.-i.; Yamashita, Y. Novel Donor−π−Acceptor Compounds Containing 1,3-Dithiol-2-ylidene and Tetracyanobutadiene Units. *Chem. Lett.* **2004**, *33*, 1190−1191.

(54) Michinobu, T.; May, J. C.; Lim, J. H.; Boudon, C.; Gisselbrecht, J. P.; Seiler, P.; Gross, M.; Biaggio, I.; Diederich, F. A new class of organic donor-acceptor molecules with large third-order optical nonlinearities. *Chem. Commun.* **2005**, *36*, 737−739.

(55) Kato, S.; Diederich, F. Non-planar push-pull chromophores. *Chem. Commun.* **2010**, *46*, 1994−2006.

(56) Jayamurugan, G.; Gisselbrecht, J. P.; Boudon, C.; Schoenebeck, F.; Schweizer, W. B.; Bernet, B.; Diederich, F. Expanding the chemical space for push-pull chromophores by non-concerted [2+2] and [4+2] cycloadditions: access to a highly functionalised 6,6-dicyanopentafulvene with an intense, low-energy charge-transfer band. *Chem. Commun.* **2011**, *47*, 4520−4522.

(57) Reisinger, C. M.; Rivera-Fuentes, P.; Lampart, S.; Schweizer, W. B.; Diederich, F. Cascade pericyclic reactions of alleno-acetylenes:

facile access to highly substituted cyclobutene, dendralene, pentalene, and indene skeletons. *Chem. Eur. J.* **2011**, *17*, 12906−12911.

(58) Michinobu, T.; Seo, C.; Noguchi, K.; Mori, T. Effects of click postfunctionalization on thermal stability and field effect transistor performances of aromatic polyamines. *Polym. Chem.* **2012**, *3*, 1427−1435.

(59) Jayamurugan, G.; Finke, A. D.; Gisselbrecht, J. P.; Boudon, C.; Schweizer, W. B.; Diederich, F. One-pot access to push-pull oligoenes by sequential [2 + 2] cycloaddition-retroelectrocyclization reactions. *J. Org. Chem.* **2014**, *79*, 426−431.

(60) Reekie, T. A.; Donckele, E. J.; Manenti, G.; Puntener, S.; Trapp, N.; Diederich, F. A Three-Step Synthesis of Tetrasubstituted NH-Pyrroles. *Org. Lett.* **2016**, *18*, 2252−2255.

(61) Shoji, T.; Ito, S. Azulene-Based Donor-Acceptor Systems: Synthesis, Optical, and Electrochemical Properties. *Chem. Eur. J.* **2017**, *23*, 16696−16709.

(62) Park, J. S.; Park, J.; Yang, Y. J.; Tran, T. T.; Kim, I. S.; Sessler, J. L. Disparate Downstream Reactions Mediated by an Ionically Controlled Supramolecular Tristate Switch. *J. Am. Chem. Soc.* **2018**, *140*, 7598−7604.

(63) Shoji, T.; Takagaki, S.; Ariga, Y.; Yamazaki, A.; Takeuchi, M.; Ohta, A.; Sekiguchi, R.; Mori, S.; Okujima, T.; Ito, S. Molecular Transformation to Pyrroles, Pentafulvenes, and Pyrrolopyridines by [2+2] Cycloaddition of Propargylamines with Tetracyanoethylene. *Chem. Eur. J.* **2020**, *26*, 1931−1935.

(64) Srinivasa Rao, P.; Brixi, S.; Shaikh, D. B.; Al Kobaisi, M.; Lessard, B. H.; Bhosale, S. V.; Bhosale, S. V. The Effect of TCNE and TCNQ Acceptor Units on Triphenylamine-Naphthalenediimide Push-Pull Chromophore Properties. *Eur. J. Org. Chem.* **2021**, *2021*, 2615−2624.

(65) Mateo, L. M.; Sagresti, L.; Luo, Y.; Guldi, D. M.; Torres, T.; Brancato, G.; Bottari, G. Expanding the Chemical Space of Tetracyanobuta-1,3-diene (TCBD) through a Cyano-Diels-Alder Reaction: Synthesis, Structure, and Physicochemical Properties of an Anthryl-fused-TCBD Derivative. *Chem. Eur. J.* **2021**, *27*, 16049−16055.

(66) Erden, K.; Dengiz, C. 3-Alkynylindoles as Building Blocks for the Synthesis of Electronically Tunable Indole-Based Push-Pull Chromophores. *J. Org. Chem.* **2022**, *87*, 4385−4399.

(67) Huang, S.; Ma, J.; Yi, Y.; Li, M.; Cai, P.; Wu, N. Synthesis of orthogonal push-pull chromophores via click reaction of arylynamines. *Org. Biomol. Chem.* **2022**, *20*, 4081−4085.

(68) Hu, X.; Lin, Z.; Wang, S.; Zhang, G.; Lin, S.; Huang, T.; Chen, R.; Chung, L.-H.; He, J. Highly Crystalline Flower-Like Covalent-Organic Frameworks Enable Highly Stable Zinc Metal Anodes. *ACS Appl. Energy Mater.* **2022**, *5*, 3715−3723.

(69) Kang, C.; Zhang, Z.; Wee, V.; Usadi, A. K.; Calabro, D. C.; Baugh, L. S.; Wang, S.; Wang, Y.; Zhao, D. Interlayer Shifting in Two-Dimensional Covalent Organic Frameworks. *J. Am. Chem. Soc.* **2020**, *142*, 12995−13002.

(70) Kang, C.; Yang, K.; Zhang, Z.; Usadi, A. K.; Calabro, D. C.; Baugh, L. S.; Wang, Y.; Jiang, J.; Zou, X.; Huang, Z.; Zhao, D. Growing single crystals of two-dimensional covalent organic frameworks enabled by intermediate tracing study. *Nat. Commun.* **2022**, *13*, 1370.

(71) Kivala, M.; Boudon, C.; Gisselbrecht, J. P.; Seiler, P.; Gross, M.; Diederich, F. Charge-transfer chromophores by cycloaddition-retroelectrocyclization: multivalent systems and cascade reactions. *Angew. Chem., Int. Ed.* **2007**, *46*, 6357−6360.

(72) Kivala, M.; Boudon, C.; Gisselbrecht, J. P.; Enko, B.; Seiler, P.; Muller, I. B.; Langer, N.; Jarowski, P. D.; Gescheidt, G.; Diederich, F. Organic super-acceptors with efficient intramolecular charge-transfer interactions by [2+2] cycloadditions of TCNE, TCNQ, and F4-TCNQ to donor-substituted cyanoalkynes. *Chem. Eur. J.* **2009**, *15*, 4111−4123.

(73) Kato, S.; Kivala, M.; Schweizer, W. B.; Boudon, C.; Gisselbrecht, J. P.; Diederich, F. Origin of intense intramolecular charge-transfer interactions in nonplanar push-pull chromophores. *Chem. Eur. J.* **2009**, *15*, 8687−8691.

(74) Silvestri, F.; Jordan, M.; Howes, K.; Kivala, M.; Rivera-Fuentes, P.; Boudon, C.; Gisselbrecht, J. P.; Schweizer, W. B.; Seiler, P.; Chiu, M.; Diederich, F. Regular acyclic and macrocyclic [AB] oligomers by formation of push-pull chromophores in the chain-growth step. *Chem. Eur. J.* **2011**, *17*, 6088−6097.

(75) Tang, X.; Chen, Z.; Xu, Q.; Su, Y.; Xu, H.; Horike, S.; Zhang, H.; Li, Y.; Gu, C. Design of Photothermal Covalent Organic Frameworks by Radical Immobilization. *CCS Chem* **2022**, *4*, 2842−2853.

(76) Monti, F.; Venturini, A.; Nenov, A.; Tancini, F.; Finke, A. D.; Diederich, F.; Armaroli, N. Anilino-Substituted Multicyanobuta-1,3-diene Electron Acceptors: TICT Molecules with Accessible Conical Intersections. *J. Phys. Chem. A* **2015**, *119*, 10677−10683.

(77) Bui, A. T.; Philippe, C.; Beau, M.; Richy, N.; Cordier, M.; Roisnel, T.; Lemiegre, L.; Mongin, O.; Paul, F.; Trolez, Y. Synthesis, characterization and unusual near-infrared luminescence of 1,1,4,4-tetracyanobutadiene derivatives. *Chem. Commun.* **2020**, *56*, 3571−3574.

(78) Chen, G.; Sun, J.; Peng, Q.; Sun, Q.; Wang, G.; Cai, Y.; Gu, X.; Shuai, Z.; Tang, B. Z. Biradical-Featured Stable Organic-Small-Molecule Photothermal Materials for Highly Efficient Solar-Driven Water Evaporation. *Adv. Mater.* **2020**, *32*, No. e1908537.

(79) Jin, Y.; Zhang, T.; Zhao, J.; Zhao, Y.; Liu, C.; Song, J.; Hao, X.; Wang, J.; Jiang, K.; Fan, S.; Li, Q. Spray coating of a perfect absorber based on carbon nanotube multiscale composites. *Carbon* **2021**, *178*, 616−624.

(80) Rathod, T. D.; Sahu, S. K.; Tiwari, M.; Bhangare, R. C.; Ajmal, P. Y. Light absorption enhancement due to mixing in black carbon and organic carbon generated during biomass burning. *Atmos. Pollut. Res.* **2021**, *12*, 101236.

(81) Liu, D.; Lei, C.; Wu, K.; Fu, Q. A Multidirectionally Thermoconductive Phase Change Material Enables High and Durable Electricity via Real-Environment Solar-Thermal-Electric Conversion. *ACS Nano* **2020**, *14*, 15738−15747.

(82) Gao, Y.; Zhang, M.; Cui, Y.; Bao, D.; Xu, F.; Shen, X.; Zhu, Y.; Wang, H. A hierarchical thermal interface material based on a double self-assembly technique enables efficient output power via solar thermoelectric conversion. *J. Mater. Chem. A* **2022**, *10*, 10452−10465.

(83) Yang, J.; Tang, L.-S.; Bao, R.-Y.; Bai, L.; Liu, Z.-Y.; Yang, W.; Xie, B.-H.; Yang, M.-B. An ice-templated assembly strategy to construct graphene oxide/boron nitride hybrid porous scaffolds in phase change materials with enhanced thermal conductivity and shape stability for light−thermal−electric energy conversion. *J. Mater. Chem. A* **2016**, *4*, 18841−18851.

(84) Yang, J.; Yu, P.; Tang, L. S.; Bao, R. Y.; Liu, Z. Y.; Yang, M. B.; Yang, W. Hierarchically interconnected porous scaffolds for phase change materials with improved thermal conductivity and efficient solar-to-electric energy conversion. *Nanoscale* **2017**, *9*, 17704−17709.

(85) Yang, J.; Tang, L.-S.; Bao, R.-Y.; Bai, L.; Liu, Z.-Y.; Yang, W.; Xie, B.-H.; Yang, M.-B. Largely enhanced thermal conductivity of poly (ethylene glycol)/boron nitride composite phase change materials for solar-thermal-electric energy conversion and storage with very low content of graphene nanoplatelets. *Chem. Eng. J.* **2017**, *315*, 481−490.

(86) Yang, J.; Tang, L.-S.; Bai, L.; Bao, R.-Y.; Liu, Z.; Xie, B.-H.; Yang, M.-B.; Yang, W. Photodriven Shape-Stabilized Phase Change Materials with Optimized Thermal Conductivity by Tailoring the Microstructure of Hierarchically Ordered Hybrid Porous Scaffolds. *ACS Sustainable Chem. Eng.* **2018**, *6*, 6761−6770.

(87) Niu, Z.; Yuan, W. Highly Efficient Thermo- and Sunlight-Driven Energy Storage for Thermo-Electric Energy Harvesting Using Sustainable Nanocellulose-Derived Carbon Aerogels Embedded Phase Change Materials. *ACS Sustainable Chem. Eng.* **2019**, *7*, 17523−17534.

(88) Wu, G.; Bing, N.; Li, Y.; Xie, H.; Yu, W. Three-dimensional directional cellulose-based carbon aerogels composite phase change materials with enhanced broadband absorption for light-thermal-electric conversion. *Energy Convers. Manag.* **2022**, *256*, 115361.